International Journal of Precision Engineering and Manufacturing (2024) 25:981–993
https://doi.org/10.1007/s12541-024-00963-3

Online ISSN 2005-4602
Print ISSN 2234-7593

REGULAR PAPER

An Active Geophone Sensor with Optimized State Variable Filter for Measuring Low-Band Frequencies

Jinsoo Choi[1] · Hongki Yoo[1] · Eunjong Choi[2] · Kihyun Kim[2] · Hyo-Young Kim[2]

Received: 12 July 2023 / Revised: 9 January 2024 / Accepted: 10 January 2024 / Published online: 6 February 2024

Abstract

An active vibration-isolation system (AVIS) utilizes a geophone sensor, a type of velocity sensor, to control microvibration. The structure of the sensor is modeled by mass, damper, and spring. The mathematical model of the geophone sensor is a second-order model with a resonant frequency. However, at low-band frequencies, the response characteristic is nonlinear and phase delay occurs. Compared with the ideal velocity signals of the system, the velocity signals measured from the geophone sensor were distorted in low-band frequencies. Consequently, this measurement issue in feedback control loops can affect the stability and performance of the AVIS. This paper proposes design rules for a state-variable filter (SVF) that can compensate for the nonlinearity of the geophone sensors in low-band frequencies and evaluates vibration attenuation performance of the AVIS by applying the proposed SVF. To evaluate the effectiveness of the filter in compensating for the nonlinear response of the geophone sensor, we compared Bode plots generated through simulation and experimental results obtained using a dynamic signal analyzer. The experimental results demonstrated that the proposed SVF effectively reduces the resonance peak of the geophone sensor and expands the frequency bands that maintain a constant magnitude in range of 0.8–10 Hz. By applying the geophone sensor with SVF to AVIS, the microvibration attenuation improved to − 18.4 dB near 4.5 Hz.

Keywords State variable filter · Active vibration-isolation system · Geophone sensor · Low-frequency compensation · Vibration measurement

1 Introduction

Active vibration-isolation systems (AVISs) are commonly used to attenuate microvibrations in various fields, including the semiconductor industry, microscopy, and high-precision measurement systems [1–4]. Although passive vibration-isolation systems (PVIS) do not require sensors or actuators, they cannot guarantee vibration-isolation performance near the resonant frequency. Therefore, AVISs are required to improve the microvibration attenuation performance at the resonant frequency [5–9]. In particular, the geophone sensor, which have features such as cost effectiveness, light weight, simple structure, and high tensile strength has been commonly used as a velocity sensor in AVIS. Ding et al. [10] analyzed the signal to noise ratio of geophone sensors used in AVIS and improved performance by dividing and controlling the frequency bands. Tonoli et al. [11] specifically analyzed the performance of AVIS which has voice coil motor and geophone sensor based on simulation and experiment. Laro et al. [12] analyzed the tilt-horizontal coupling problem of geophone sensors used in AVIS and proposed a solution.

However, the geophone sensor faces problems with low-frequency responses owing to its mechanical–electrical structure [13]. The mathematical model of the geophone sensor is a second-order model with a mass, damper, and spring. The zeros are close to origin on the complex s-plane than the poles. Therefore, it has a slope in the low-band frequencies, resulting in distorted velocity signals from the geophone sensor because of nonlinearity. Therefore, the response of the geophone sensor cannot maintain a constant magnitude, resulting in a nonlinear section in the low-frequency band. Therefore, the signal-to-noise ratio deteriorates in a microvibration, making improvement of control

✉ Kihyun Kim
khkim12@tukorea.ac.kr

✉ Hyo-Young Kim
kimhy@tukorea.ac.kr

1 Department of Mechanical Engineering, Korea Advanced Institute of Science and Technology, Daejeon, Korea

2 Department of Mechatronics Engineering, Tech University of Korea, Siheung, Korea

performance difficult. The resonant frequency of AVIS is designed to be in the low-band frequencies. The control performance degrades in the bandwidth of the feedback control loop because the response at the resonant frequency (low-frequency section) of AVIS is output smaller than the actual response, thereby affecting the stability and control performance of AVISs with respect to the microvibration attenuation [14–19]. Consequently, the controller operates based on a distorted velocity signal and margin of the designed controller may not be ideal [20–22]. Although these problems are resolved using a low gain, the performance may degrade in AVISs. To improve the signal measured by the sensors, various approaches such as multi-sensor [23–26], sensor-less control [27], signal conditioning circuit [28], and modified electromechanical system [29–31], specially designed sensor [32, 33] have been proposed. In addition, research on combining a sensor and a filter for maintaining constant-magnitude response has been proposed; however, the method of designing a circuit differs depending on the model of the sensor [34, 35].

This study proposes design rules for a state-variable filter (SVF) to enhance the low-band frequencies of geophone sensors in AVISs for high-performance vibration control. The SVF, which is an active filter, comprises a capacitor, resistor and operational amplifier; it employs a state feedback structure that analyzes the response characteristics through state-space modeling for current operational amplifiers or enhanced piezoelectric properties, such as signal-to-noise ratio, sensitivity, and maintaining a constant-magnitude response [36, 37]. Previous studies have attempted to improve frequency characteristics; however, the AVIS system presented in this study requires a further improved low-frequency band. An SVF can be represented as a linear combination of a high-pass filter (HPF), bandpass filter (BPF), and low-pass filter (LPF). The signal output of each filter becomes a state variable, resulting in a second-order system. The SVF can adjust the cutoff frequency and damping ratio independently; these can be determined by assuming that the specific element values used in SVF have the same value and must meet a certain ratio [38]. Additionally, the damping ratio can be adjusted using specific resistor values. Analog filters typically take into account the coupling issues of circuit component values owing to their response characteristics. Consequently, an SVF offers a more flexible circuit design by adjusting the cutoff frequency and damping ratio independently. By applying SVF to a geophone sensor for resonant frequency reduction and low-frequency amplification, new design rules suitable for enhancing the vibration-isolation performance of AVISs are obtained. To evaluate the compensation for nonlinear response of the geophone sensor using SVFs, we compared Bode plots obtained from experimental results with dynamic signal analyzer (DSA). The experimental results demonstrated that the proposed SVF effectively reduces the resonance peak of geophone sensors and expands the frequency bands that maintain a constant magnitude ranging from 0.8 to 10 Hz. By applying the geophone sensor with SVF to an AVIS, the microvibration attenuation improved to − 18.4 dB near 4.5 Hz.

The remainder of this paper is organized as follows. In Sect. 2, the effect of the compensation range on the plant is evaluated through simulations combining the plant and geophone sensor models. Section 3 describes the fabrication of an analog circuit design of the SVF based on a mathematical model and evaluates the resonance peak attenuation and extension of the range that maintaining constant-magnitude response. Section 4 presents the experimental results of microvibration attenuation of the geophone sensor with SVF to validate the improved control performance of the AVIS. Finally, Sect. 5 concludes the study.

2 Modeling and Simulation of Nonlinear Response Compensation

2.1 Electromechanical Modeling of Geophone Sensor

The proposed velocity sensor is a geophone sensor GS-11D, which converts velocity into electrical signals. When floor vibrations are transmitted to the geophone sensor surface, an electromotive force is generated inside the coil owing to the interaction between the permanent magnet and coil according to the Faraday's law. The magnitude of the electromotive force represents the linear characteristics of the time derivatives of the magnetic flux density. Subsequently, the magnitude of the velocity was predicted by measuring the voltage using the geophone sensor [39–41].

$$m_s\ddot{x}_m + c_s(\dot{x}_m - \dot{x}_g) + k_s(x_m - x_g) + G_S\dot{q} = 0 \tag{1}$$

$$m_s\ddot{x}_s + c_s\dot{x}_s + k_s x_s + G_s\dot{q} = -m_s\ddot{x}_g \tag{2}$$

Equations (1) and (2) represent the mathematical models of the mechanical parts, and Fig. 1 shows that electromotive force $G_S\dot{q}$ is generated according to the Faraday's law owing to the relative displacement $x_s = x_m - x_g$ of the floor vibration x_g and displacement x_m of the inertia mass m_s. The relationship between the magnet and the inertia mass can be expressed in terms of the damping coefficient c_s and spring constant k_s. V_0 is the magnitude of the electrical output generated by the geophone sensor, and q is the charge. G_s is a constant proportional to the magnetic flux density and has units [V/(m/s)]. Equation (3), which indicates the electrical component, can be obtained using the following second-order differential equation:

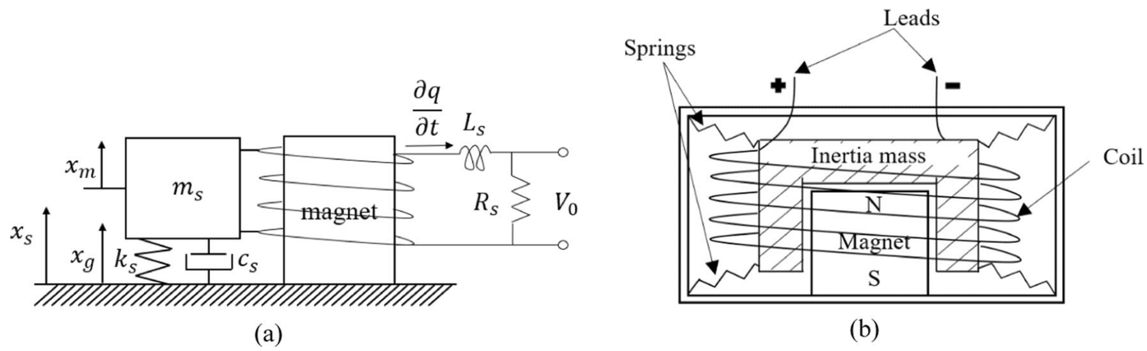

Fig. 1 **a** Electromechanical schematic and **b** structure of geophone sensor

$$L_s\ddot{q} + R_s\dot{q} - G_s\dot{x}_s = 0. \tag{3}$$

Equations (2) and (3) can be expressed using the Laplace transform **L** (assumption that all of the initial condition is zero and variables q, x_s, x_g, and x_m related to time derivatives are changed to Q, X_s, X_g, and X_m), respectively, as follows:

$$m_s s^2 X_s + c_s s X_s + k_s X_s + G_s s Q = -m_s s^2 X_g \tag{4}$$

$$L_s s^2 Q + R_s s Q - G_s s X_s = 0 \tag{5}$$

By combining Eqs. (4) and (5), the output X_s can be expressed as Eq. (6).

$$m_s s^2 X_s + c_s s X_s + k_s X_s + \frac{G_s^2 s X_s}{L_s s + R_S} = -m_s s^2 X_g \tag{6}$$

Here, the interaction between the motion of the coil and permanent magnet can be expressed using the Faraday's Law of electromagnetic induction. The geophone has a similar structure to the voice coil transducer, the induced electromotive force of the coil can be expressed as the relative velocity between the coil and the magnet. A voice coil transducer converts electrical and mechanical energy into each other. Let the relative velocity of the coil and the permanent magnet be v, the external force that maintains equilibrium with the electromagnetic force is f, the number of turns of coil is n, the potential difference between both ends of the coil is ε, and the electric current in the coil is i. This transducer follows Faraday's law $\varepsilon = 2\pi nrBv = Tv$. T is transducer constant. x_s is the relative displacement of the coil and permanent magnet, and G_s is the sensitivity of the sensor. Therefore, the induced electromotive force of the coil can be expressed as follow:

$$V_0 = -G_s s X_s \tag{7}$$

Equation (8) is obtained by combining Eqs. (6) and (7) for the voltage output V_0 with the applied displacement X_g. sX_g is the speed of floor vibration and is the Laplace transform expression of the differential of displacement X_g.

$$\frac{V_0}{sX_g} = \frac{m_s G_s s^2}{m_s s^2 + c_s s + k_s + \frac{G_s^2 s}{L_s s + R_s}} \tag{8}$$

If R_s is large, Eq. (8) is reduced to:

$$\frac{V_0}{sX_g} \approx \frac{G_s s^2}{s^2 + \frac{c_s}{m_s} s + \frac{k_s}{m_s}} \tag{9}$$

The transfer function in Eq. (9) can be expressed as Eq. (10) by substituting the parameters presented in Table 1. The table was filled based on the datasheet provided by the geophone sensor manufacturer and includes the parameters and sensitivities. Additionally, the specifications of elements were measured at a vibration input of 100 Hz or less.

$$\frac{V_0}{sX_g} = \frac{G_s s^2}{s^2 + \frac{c_s}{m_s} s + \frac{k_s}{m_s}} = \frac{32s^2}{s^2 + 18s + 760} \tag{10}$$

The frequency response obtained from the geophone sensor model shown in Fig. 2 indicates that a resonant frequency is 4.5 Hz and nonlinearity is occurred at low-band frequencies (below 10 Hz). This nonlinear response

Table 1 Specifications of the geophone sensor (GS-11D)

Properties	Symbols	Values
Resonant frequency	$\frac{1}{2\pi}\sqrt{\frac{k_s}{m_s}}$	4.5 ± 0.75 (Hz)
Damping coefficient	c_s	0.34 ± 20% (Ns/m)
Inertia mass	m_s	23.6 ± 5% (g)
Sensitivity gain	G_s	32 ± 10% (V/(m/s))
DC Coil resistance @25 °C	R_s	380 ± 5% (Ω)
Maximum coil excursion p–p	$\max(x_s)$	2.5 (mm)
Coil inductance	L_s	50 ± 5% (mH)

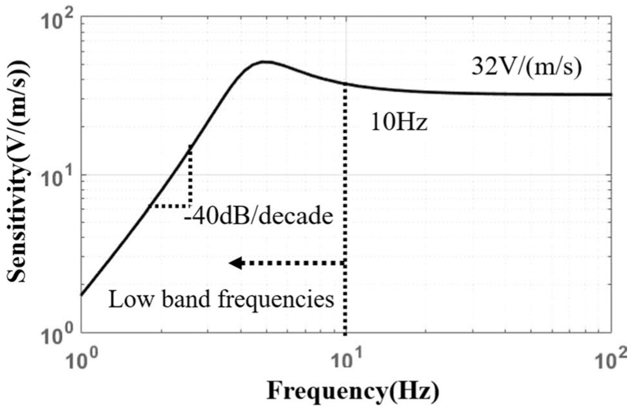

Fig. 2 Frequency response of the geophone sensor (GS-11D)

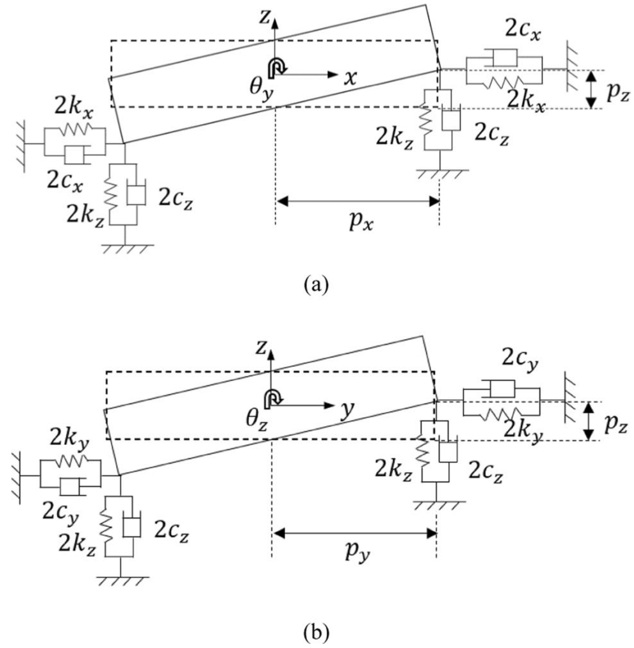

Fig. 3 Modeling for passive vibration-isolation system: **a** X–Z Plane, **b** Y–Z Plane

causes errors between the velocity signal measured by the geophone sensor and system's actual behavior, leading to performance degradation and changes in the design margins for the AVIS controller. To mitigate this performance degradation, we propose an SVF to improve the responsiveness in low-band frequencies and verify the designed SVF by applying it to the AVIS. Section 2.2 describes the plant-modeling process.

2.2 Modeling of AVIS

Equations (11)–(16) present the mathematical model of the AVIS. This plant includes the mass m (upper plate and stage), damping coefficient $c_i(i = x, y, z)$, spring constant $k_i(i = x, y, z)$, moment of inertia $i_i(i = x, y, z)$, axial displacement of the upper plate $x_p, y_p, z_p, \theta_{xp}, \theta_{yp}, \theta_{zp}$, axial displacement of the ground $x_b, y_b, z_b, \theta_{xb}, \theta_{yb}, \theta_{zb}$, input force/moment $F_i/M_{\theta_i}(i = x, y, z)$ and distance between the center of gravity and isolator $p_i(i = x, y, z)$ can be modeled as a second-order system in Fig. 3 [40–42]. The six degrees-of-freedom system was analyzed on the z-axis only to study the performance of the SVF. Table 2 lists the specifications of the experimental parts.

$$\begin{aligned} F_x(t) = & m\ddot{x}_p(t) + c_x\left(\dot{x}_p(t) - \dot{x}_b(t)\right) \\ & + k_x\left(x_p(t) - x_b(t)\right) \\ & - c_x p_z \dot{\theta}_{yp}(t) - k_x p_z \theta_{yp}(t) \end{aligned} \tag{11}$$

$$\begin{aligned} F_y(t) = & m\ddot{y}_p(t) + c_y\left(\dot{y}_p(t) - \dot{y}_b(t)\right) \\ & + k_y\left(y_p(t) - y_b(t)\right) \\ & - c_y p_z \dot{\theta}_{xp}(t) - k_y p_z \theta_{xp}(t) \end{aligned} \tag{12}$$

$$F_z(t) = m\ddot{z}_p(t) + c_z\left(\dot{z}_p(t) - \dot{z}_b(t)\right) + k_z\left(z_p(t) - z_b(t)\right) \tag{13}$$

$$\begin{aligned} M_{\theta_x}(t) = & i_{xx}\ddot{\theta}_{xp}(t) + \left(c_z p_y^2 + c_y p_z^2\right)\left(\dot{\theta}_{xp}(t) - \dot{\theta}_{xb}(t)\right) \\ & + \left(k_y p_z^2 + k_z p_y^2\right)\left(\theta_{xp}(t) - \theta_{xb}(t)\right) \\ & + c_y p_z \dot{y}_p(t) + k_y p_z y_p(t) \end{aligned} \tag{14}$$

$$\begin{aligned} M_{\theta_y}(t) = & i_{yy}\ddot{\theta}_{yp}(t) + \left(c_x p_z^2 + c_z p_x^2\right)\left(\dot{\theta}_{yp}(t) - \dot{\theta}_{yb}(t)\right) \\ & + \left(k_x p_z^2 + k_z p_x^2\right)\left(\theta_{yp}(t) - \theta_{yb}(t)\right) \\ & - c_x p_z \dot{x}_p(t) - k_x p_z x_p(t) \end{aligned} \tag{15}$$

$$\begin{aligned} M_{\theta_z}(t) = & i_{zz}\ddot{\theta}_{zp}(t) + \left(c_x p_y^2 + c_y p_x^2\right)\left(\dot{\theta}_{zp}(t) - \dot{\theta}_{zb}(t)\right) \\ & + \left(k_x p_y^2 + k_y p_x^2\right)\left(\theta_{zp}(t) - \theta_{zb}(t)\right) \end{aligned} \tag{16}$$

2.3 Simulation Results for Low-Band Frequencies with Respect to Compensation Range of SVF

An inverse transfer function of the geophone sensor for maintaining a constant-magnitude response causes instability, as

Table 2 Specifications of experimental parts

Type	Model	Parameter	Value
Controller	DS1005	Serial interface	RS232/115.2 Kbaud
		Sampling frequency	10 kHz
AD/DA converter	DS2003/DS2103	voltage range	± 10 V
		Resolution	16 bit
Actuator	Voice coil motor	Force constant	59 N/A
Actuator amplifier	TA115	Bandwidth	4 kHz
		Force gain	0.2–0.8 A/V
Position sensor+	EX-422	Measuring range	0 to 10 mm
		Linearity	1% of F.S
		Response frequency	1.3 kHz (− 3 dB)

shown in Eq. (10), because zeros exist at the origin of the s-plane. Therefore, a compensation range is required to improve the nonlinearity of the sensor response. However, the compensation range is significantly affected by the values of the circuit components. Generally, the capacitances are of the order of a few microfarads; thus, high capacitance and resistance values are impractical. Therefore, limiting the compensation range for low-band frequencies is necessary for using practical capacitance and resistance values. In this study, capacitance and resistance of a compensation range for

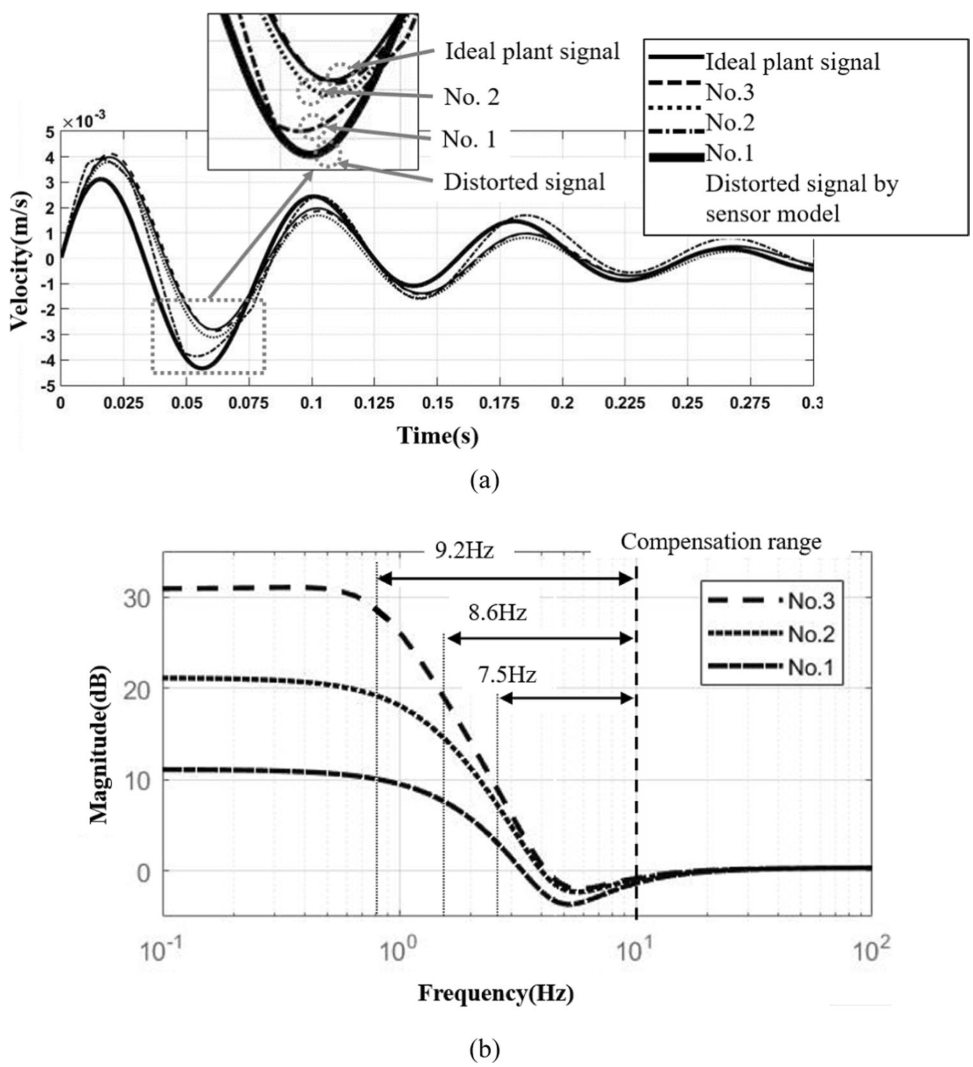

Fig. 4 Time-domain simulation results with respect to compensation range with **a** results in time domain and **b** Bode plots

maintaining a constant-magnitude response was proposed to be less than 1 μF and 1 MΩ. The output error according to the compensation range was calculated using Eq. (17). The time-domain responses for each compensation range based on the three cases are shown in Fig. 4. The plant model represents the ideal output of the plant, whereas the uncompensated model represents a signal that is distorted by including the sensor model in the plant model. The numbers (No.) represent the output of the plant model with the sensor model and SVF with respect to the compensation range listed in Table 3. When the compensation range increases, the compensated signal of the plant approximates the ideal signal. The error between the ideal signal and compensated signal of the plant is expressed as follows:

$$error = \left(\left| \frac{\text{plant model area} - \text{compensated model area}}{\text{plant model area}} \right| \right) \tag{17}$$

Here, the transfer function (TF_{comp}) of SVF model should satisfy the following three conditions: $TF_{comp\ s\to\infty} \approx 0$ dB, locations of zero at 4.5 Hz, and a second-order system. In this study, compensation range No. 3 was selected, which matched about 92% of the ideal signal of the plant, and a second-order compensation filter that satisfied the slope and magnitude conditions was chosen. The Bode plot of the proposed SVF that satisfies the previously mentioned conditions is the same as that of No. 3, and the transfer function is given by Eq. (18).

Table 3 Errors between the ideal and distorted signals with respect to compensation range

Case 1	Ideal plant signal			
Case 2	Distorted signal by geophone sensor model			
Case 3	No. 1–3 compensated sensor signal by SVF		Compensation range (Hz)	Error (%)
		No. 1	2.5–10 (Hz)	44.11 (%)
		No. 2	1.4–10 (Hz)	25.36 (%)
		No. 3	0.8–10 (Hz)	7.51 (%)

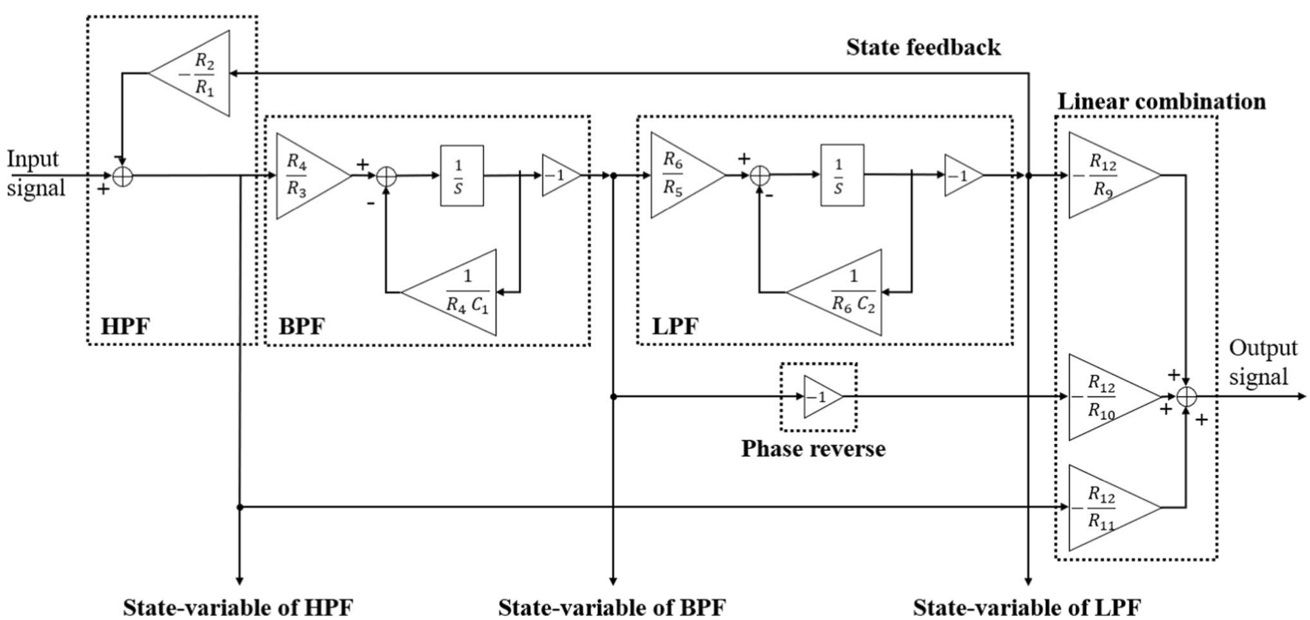

Fig. 5 Block diagram of the proposed SVF for expanding the range of constant-magnitude response of geophone sensor

Table 4 The electric circuit parameters in proposed SVF

Symbol	R_1	R_2	R_3	R_4	R_5	R_6	R_7
Value (unit)	24 (kΩ)	33 (Ω)	110 (kΩ)	1 (MΩ)	110 (kΩ)	1 (MΩ)	1 (kΩ)
Symbol	R_8	R_9	R_{10}	R_{11}	R_{12}	C_1	C_2
Value (unit)	1 (kΩ)	24 (kΩ)	12 (kΩ)	24 (kΩ)	12 (kΩ)	0.33 (μF)	0.33 (μF)

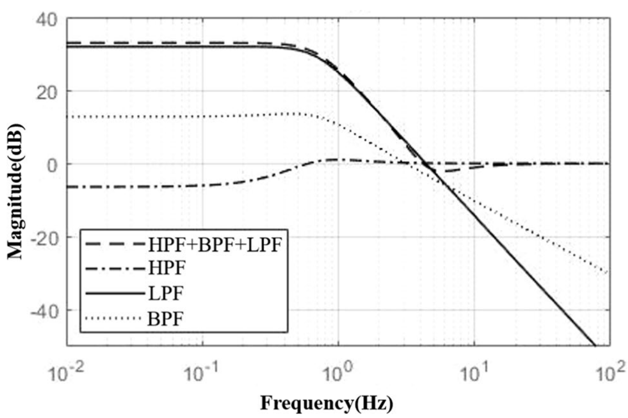

Fig. 6 Bode plots of state variable of the proposed SVF

$$TF_{comp} = -\frac{0.329s^2 + 8.072s + 280.5}{0.329s^2 + 1.997s + 6.325} \tag{18}$$

3 Analog Circuit Design for the SVF

The proposed SVF satisfies a linear combination of HPF, BPF, and LPF. Therefore, the overall transfer function can be expressed as a linear combination of the partial transfer functions, and each output can be expressed as a state variable. The total output was determined using a linear combination. Based on the state space model, a block diagram of the SVF is shown in Fig. 5. The overall transfer function satisfies Eq. (18), with the specifications listed in Table 4. Furthermore, the frequency response of each state variable can be represented as shown in Fig. 6 and defined by Eqs. (19)–(21).

The proposed analog circuit is illustrated in Fig. 7. The transfer functions of the circuit's state variables, which are expressed in Eqs. (19)–(21), are functions of resistor and capacitor. The parameters listed in Table 4 were used to determine the transfer functions.

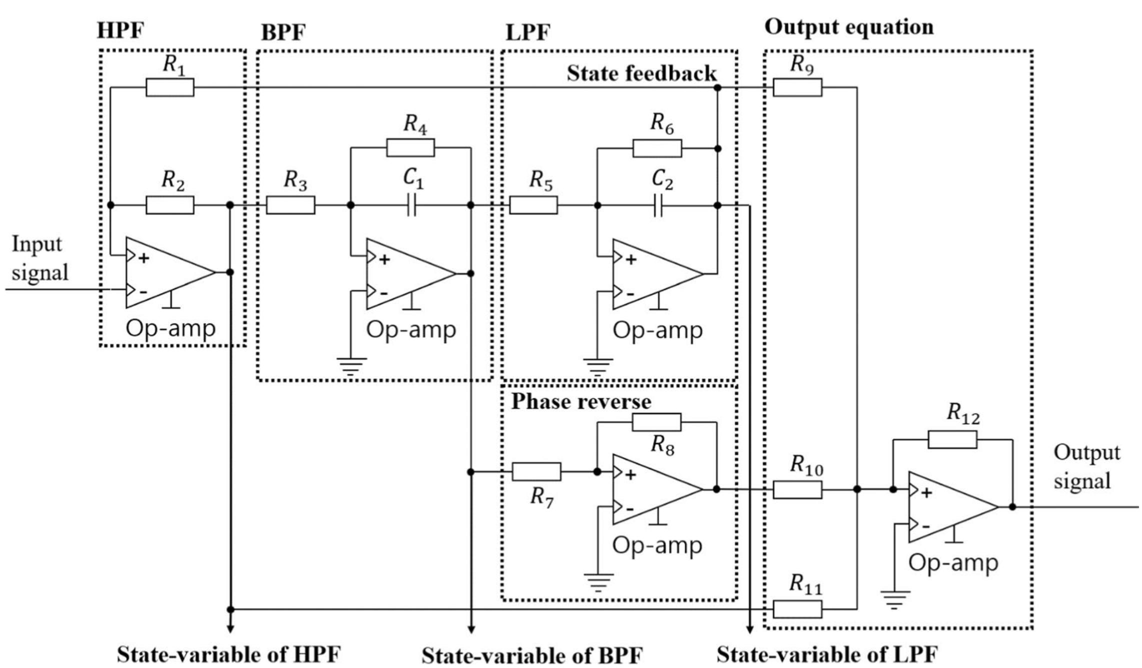

Fig. 7 Active analog circuit corresponding to Eq. (12)

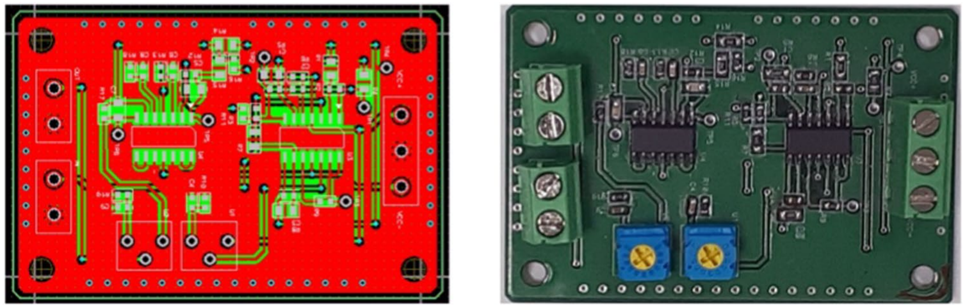

Fig. 8 Photographs of the manufactured SVF

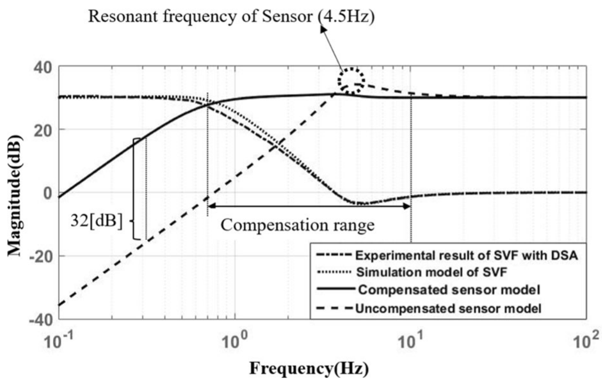

Fig. 9 Bode plots of the geophone sensor with SVF compensating for the low-band frequencies

An analog circuit based on Fig. 7 was manufactured, as shown in Fig. 8. The frequency response of the SVF was measured using an Agilent DSA 35670A, as shown in Fig. 9. As a result, the proposed filter design effectively reduced the resonance peak of the geophone sensors and expanded constant-magnitude frequency bands from 0.8 to 10 Hz.

4 Experimental Result of Microvibration Control Based on Compensated Geophone Sensor by SVF

The experimental setup for the AVIS performance evaluation is shown in Figs. 10 and 11 [43]. The control algorithm applied to the control block diagram in Fig. 12 and

$$HPF = -R_1R_3R_5\frac{(R_6C_2s+1)(R_4C_1s+1)}{R_1R_3R_5\left(R_4R_6C_1C_2s^2+(R_6C_2+R_4C_1)s+1\right)+R_2R_4R_6} = -\frac{0.329s^2+1.997s+3.025}{0.329s^2+1.997s+6.325} \tag{19}$$

$$BPF = -R_1R_4R_5\frac{R_6C_2s+1}{R_1R_3R_5\left(R_4R_6C_1C_2s^2+(R_6C_2+R_4C_1)s+1\right)+R_2R_4R_6} = -\frac{6.075s+27.5}{0.329s^2+1.997s+6.325} \tag{20}$$

$$LPF = -R_1R_4R_6\frac{1}{R_1R_3R_5\left(R_4R_6C_1C_2s^2+(R_6C_2+R_4C_1)s+1\right)+R_2R_4R_6} = -\frac{250}{0.329s^2+1.997s+6.325} \tag{21}$$

Fig. 10 System configuration in the experimental setup for the AVIS performance evaluation

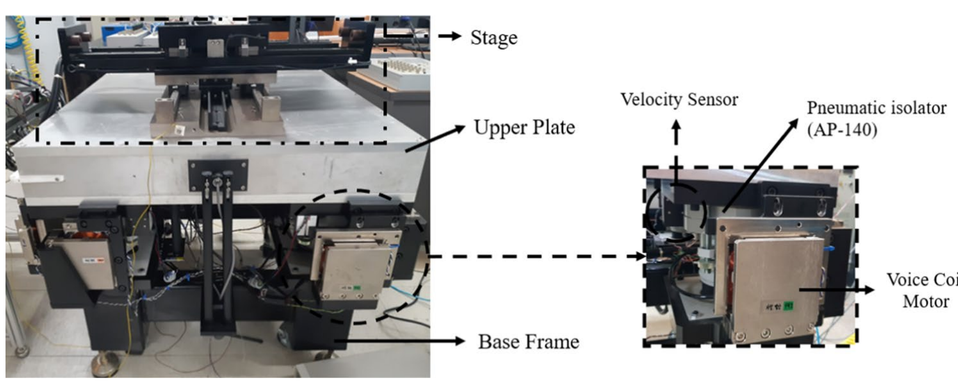

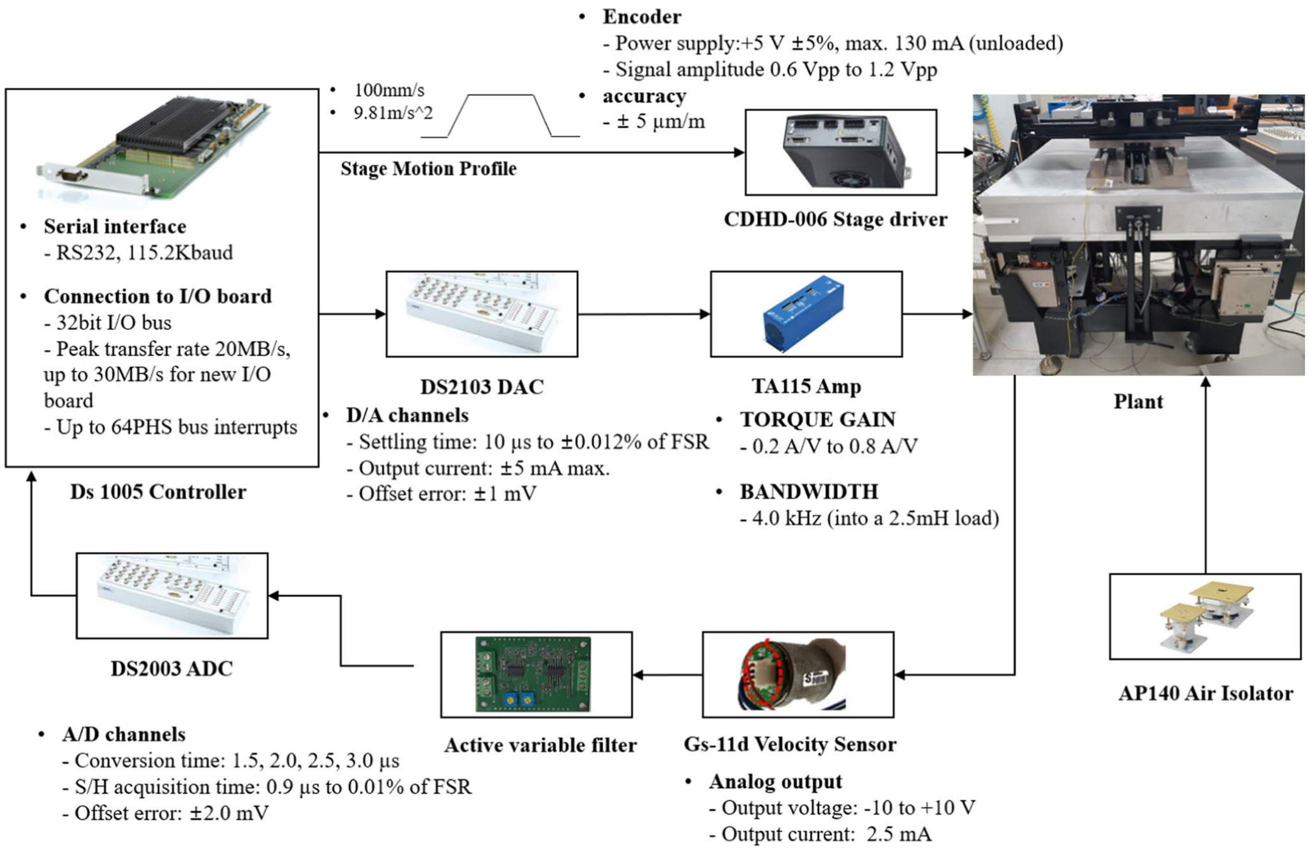

Fig. 11 Experimental setup for active vibration isolation

Fig. 12 Schematic of a state observer for the control system

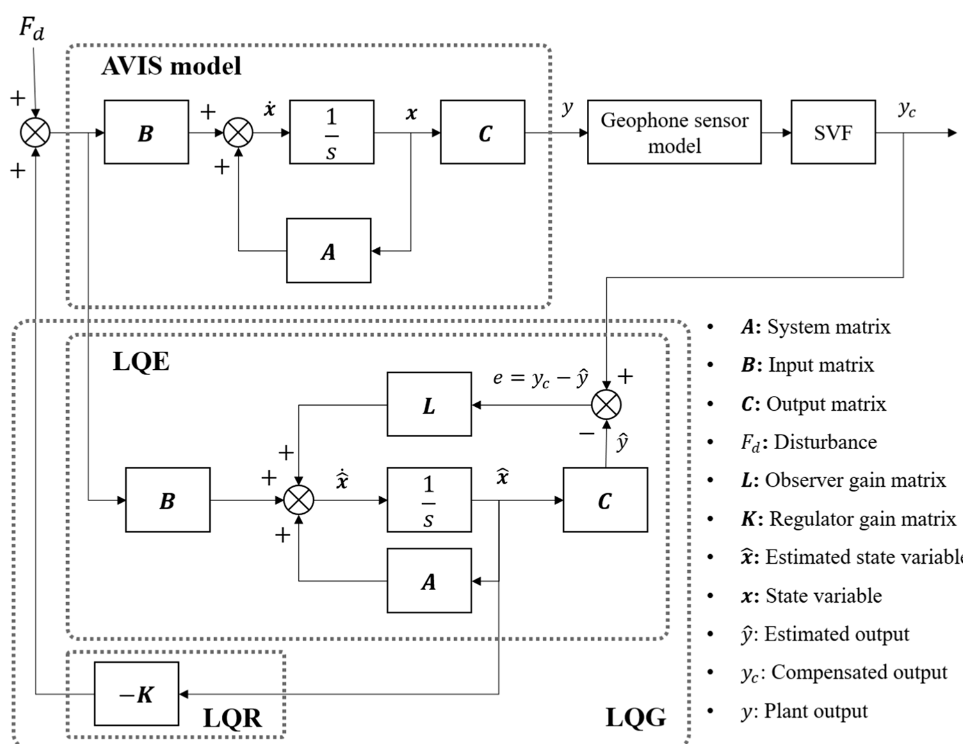

Table 5 Characteristics of linear quadratic Gaussian

	Pole placement	ω_n (rad/s)	ζ	L/K gain matrix		
Characteristic of plant model	$-8.49 \pm 42.26i$	36.5	0.233			
Characteristic of observer model	$-142 \pm 119i$	185	0.766	L	L_1	−456
					L_2	348
Characteristic of regular model	$-125 \pm 72i$	144	0.866	K	K_1	112
					K_2	130

Table 5 can be represented as a linear-quadratic Gaussian (LQG) function that consists of a linear-quadratic estimator (LQE) for estimating state variables and linear-quadratic regulator (LQR) for regulating control inputs [44–49]. Model updates are required depending on the inertia change due to moving stage. The LQG is the control algorithm based on the state space. It is easier to update the model than the traditional error-based PID controller. In this paper, the adaptive LQG controller is applied for model update. The second-order differential equation in Eqs. (11)–(16) is the system matrix $\boldsymbol{A}$; $\boldsymbol{B}$ represents the input matrix; $\boldsymbol{C}$ represents the output matrix as shown in Fig. 12. Therefore, matrices $\boldsymbol{A}$, $\boldsymbol{B}$, and $\boldsymbol{C}$ can be represented in a state space. The state variables were updated using the $\boldsymbol{L}$ gain, and the estimated state variables were fed back to control the system through the $\boldsymbol{K}$ gain. Characteristics of the observer and regulator for the $\boldsymbol{L}$, $\boldsymbol{K}$-matrix are obtained by solving the Riccati equation. Evidently, the resonance frequency (w_n) increased by three to four times and the damping ratio (ζ) also increased compared with the characteristics of the existing plant. Resonance frequency and damping ratio are related to the control bandwidth and attenuation of peak resonance. As a result, the proposed AVIS means 3–4 times faster control bandwidth and peak reduction compared with the existing PIVS. The objective of this study was to enhance the control performance by expanding the low-band frequencies and reducing the peak resonant frequency of the geophone sensor. Because the sensor output is calculated to update the state variables in the LQE, using the uncompensated sensor output as the feedback signal for the controller causes errors in the estimator. The attenuation performance can be improved using a compensated sensor output to control the system. In this section, we compare the attenuation performance of the geophone sensors with and without SVF. By applying the geophone sensor with SVF to the AVIS, the microvibration attenuation was improved to 18.4 dB near 4.5 Hz as shown in Fig. 13.

5 Conclusion

In general, the resonant frequency of an AVIS is designed to attenuate floor vibrations at low frequencies, and a geophone sensor is used to measure the velocity. Geophone sensors have the advantages of being lightweight, small, low-cost, and easy to maintain owing to their simple structure. However, when used in the AVIS, the attenuation performance degrades at the resonant frequency of the geophone sensor. These problems are caused by nonlinearity in the range of low-band frequencies.

This study designed a simulation model of an SVF to improve the performance of the low-band frequencies of geophone sensors in an AVIS. The experimental results

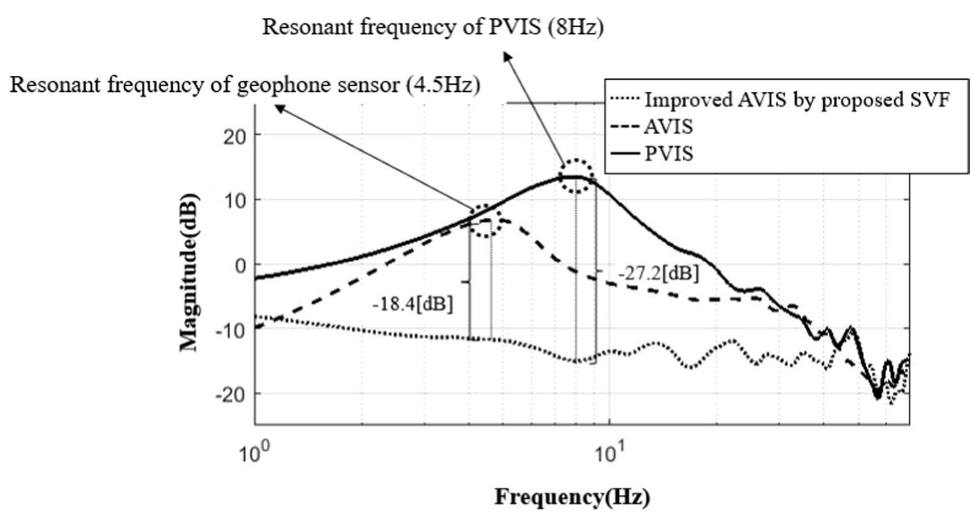

Fig. 13 Performance-result comparison of various vibration-isolation systems: passive, active, and compensated active system with the proposed SVF

demonstrated that the proposed SVF effectively reduced the resonance peak of the geophone sensors and expanded the range of constant-magnitude response from 0.8 to 10 Hz. Subsequently, the linear response range increased, and the proposed SVF was able to reduce the peak near 4.5 Hz by 18.4 dB in the AVIS. The proposed design rules enabled independent designs of the HPF, BPF, LPF, phase inversion, and linear combination. Therefore, it can also be applied to increase the linear response range of a pressure or force sensor that uses the piezoelectric effect with a resonant frequency in the high-frequency range. Consequently, the usefulness and practicality of this study was obtained in the form of filter design rules optimized for the response characteristics of various types of sensors.

Future research will be to optimize the values of the circuit elements of the SVF. In this paper, the transfer function and circuit elements were matched as Eqs. (19)–(21). Therefore, it is not difficult to obtain the transfer function and circuit elements of SVF for application to various sensors. However, there are realistic limitations to the range of values of circuit elements, and determining appropriate values of circuit elements is time-consuming. It is necessary to develop an algorithm to find the optimal values of SVF's circuit elements. If we will propose the optimization algorithm, the optimized values which have maximized flat frequency range can be proposed when limited range of values of circuit elements. As a result, the design of optimized SVFs will be automated and less time consuming.

Acknowledgements This work was supported by the GRRC program of Gyeonggi Province [(GRRC TU Korea2023-B02), Development of docking system and process technology for 3D printing post-processing automation].

References

1. Schmidt, R.-H.M. (2012). Ultraprecision engineering in lithographic exposure equipment for the semiconductor industry. *Philosophical Transactions of the Royal Society of London Series. Part A, 370*(1973), 3950–3972.
2. Li, Z., Sheng, M., Wang, M., Dong, P., Li, B., & Chen, H. (2018). Stacked dielectric elastomer actuator (SDEA): Casting process, modeling and active vibration isolation. *Smart Materials & Structures, 27*(7), 075023. https://doi.org/10.1088/1361-665X/aabea5
3. Voigtländer, B., Coenen, P., Cherepanov, V., Borgens, P., Duden, T., & Tautz, F. S. (2017). Low vibration laboratory with a single-stage vibration isolation for microscopy applications. *Review of Scientific Instruments, 88*(2), 023703. https://doi.org/10.1063/1.4975832
4. Kim, I., & Kim, Y.-S. (2009). Active vibration control of trim panel using a hybrid controller to regulate sound transmission. *International Journal of Precision Engineering & Manufacturing, 10*(1), 41–47. https://doi.org/10.1007/s12541-009-0007-2
5. Lee, J. H., Kim, H. Y., Kim, K. H., Kim, M. H., & Lee, S. W. (2017). Control of a hybrid active-passive vibration isolation system. *Journal of Mechanical Science & Technology, 31*(12), 5711–5719. https://doi.org/10.1007/s12206-017-1112-2
6. Lee, H. H., Kim, K. H., & Kim, H. Y. (2020). Development and control of a hybrid active mount module for precision stages. *Review of Scientific Instruments, 91*(2), 026101. https://doi.org/10.1063/1.5122806
7. Zhang, B., Jin, K., Kou, Y., & Zheng, X. (2019). The model of active vibration control based on giant magnetostrictive materials. *Smart Materials & Structures, 28*(8), 085028. https://doi.org/10.1088/1361-665X/ab2dd0
8. Alujević, N., Čakmak, D., Wolf, H., & Jokić, M. (2018). Passive and active vibration isolation systems using inerter. *Journal of Sound & Vibration, 418*, 163–183. https://doi.org/10.1016/j.jsv.2017.12.031
9. Ulgen, D., Ertugrul, O. L., & Ozkan, M. Y. (2016). Measurement of ground borne vibrations for foundation design and vibration isolation of a high-precision instrument. *Measurement, 93*, 385–396. https://doi.org/10.1016/j.measurement.2016.07.041
10. Ding, J., Luo, X., Chen, X., Bai, O., & Han, B. (2018). Design of active controller for low-frequency vibration isolation considering noise levels of bandwidth-extended absolute velocity sensors. *IEEE/ASME Transactions on Mechatronics, 23*(4), 1832–1842. https://doi.org/10.1109/TMECH.2018.2843558
11. Tonoli, A., Bonfitto, A., Silvagni, M., Suarez, L. D., & Zenerino, E. (2011). Active Isolation and damping of vibrations for high precision laser cutting machine. In *Vibration analysis and control-new trends and developments*. IntechOpen. https://doi.org/10.5772/25092
12. Laro, D., Van den Berg, S., Eisinger, J., & Van Eijk, J. (2011). 6-dof active vibration isolation without tilt-horizontal coupling. In *Proceedings of the 11th Euspen international conference* (pp. 15–18).
13. Oome, A. J. J. A., Janssen, J. L. G., Encica, L., Lomonova, E., & Dams, J. A. A. T. (2009). Modeling of an electromagnetic geophone with passive magnetic spring. *Sensors & Actuators Part A, 153*(2), 142–154. https://doi.org/10.1016/j.sna.2009.04.019
14. Huang, B., Kim, H. S., & Youn, B. D. (2015). Active vibration control of smart composite laminates with partial debonding of actuator. *International Journal of Precision Engineering & Manufacturing, 16*(4), 831–840. https://doi.org/10.1007/s12541-015-0109-y
15. Shin, K. (2014). On the performance of a single degree-of-freedom high-static-low-dynamic stiffness magnetic vibration isolator. *International Journal of Precision Engineering & Manufacturing, 15*(3), 439–445. https://doi.org/10.1007/s12541-014-0355-4
16. Kim, H. Y., Lee, H., Lee, S., Kim, T., & Kim, K. (2019). Design of a voice coil motor for active vibration isolator of CFRP high speed inspection system. *Journal of the Korean Society for Precision Engineering, 36*(1), 29–35. https://doi.org/10.7736/KSPE.2019.36.1.29
17. Banik, R., & Gweon, D.-G. (2007). Design and optimization of voice coil motor for application in active vibration isolation. *Sensors & Actuators Part A, 137*(2), 236–243. https://doi.org/10.1016/j.sna.2007.03.011
18. Ding, J., Wang, Y., Wang, M., Sun, Y., Peng, Y., Luo, J., & Pu, H. (2022). An active geophone with an adjustable electromagnetic negative stiffness for low-frequency vibration measurement. *Mechanical Systems & Signal Processing, 178*, 109207. https://doi.org/10.1016/j.ymssp.2022.109207

19. Chen, R., Li, X., Yang, Z., Xu, J., & Yang, H. (2021). A variable positive-negative stiffness joint with low frequency vibration isolation performance. *Measurement, 185*, 110046. https://doi.org/10.1016/j.measurement.2021.110046
20. Chen, P.-C., & Shih, M.-C. (2011). Robust control of a novel active pneumatic vibration isolator through floor vibration observer. *Journal of Vibration & Control, 17*(9), 1325–1336. https://doi.org/10.1177/1077546310361425
21. Oomen, T., van der Maas, R., Rojas, C. R., & Hjalmarsson, H. (2014). Iterative data-driven H∞ norm estimation of multivariable systems with application to robust active vibration isolation. *IEEE Transactions on Control Systems Technology, 22*(6), 2247–2260. https://doi.org/10.1109/TCST.2014.2303047
22. Burkan, R., Özgüney, Ö. C., & Özbek, C. (2018). Model reaching adaptive-robust control law for vibration isolation systems with parametric uncertainty. *Journal of Vibroengineering, 20*(1), 300–309. https://doi.org/10.21595/jve.2017.18429
23. Xiong, N., & Svensson, P. (2002). Multi-sensor management for information fusion: Issues and approaches. *Information Fusion, 3*(2), 163–186. https://doi.org/10.1016/S1566-2535(02)00055-6
24. Wang, T., Zhong, S., Luo, H., & Kuang, N. (2023). Drift error calibration method based on multi-MEMS gyroscope data fusion. *International Journal of Precision Engineering and Manufacturing, 24*(10), 1835–1844. https://doi.org/10.1007/s12541-023-00850-3
25. Cho, S., Seo, H.-R., Lee, G., Choi, S.-K.C., & Hae-Jin. (2023). A rapid learning model based on selected frequency range spectral subtraction for the data-driven fault diagnosis of manufacturing systems. *International Journal of Precision Engineering and Manufacturing-Smart Technology, 1*, 49–62. https://doi.org/10.57062/ijpem-st.2022.0031
26. Kim, E., Yun, H., Araujo, O. C., & Jun, M. B. (2023). Sound recognition based on convolutional neural network for real-time cutting state monitoring of tube cutting machine. *International Journal of Precision Engineering and Manufacturing-Smart Technology, 1*(1), 1–18. https://doi.org/10.57062/ijpem-st.2022.0038
27. Su, G.-J., & Mckeever, J. W. (2004). Low-cost sensorless control of brushless DC motors with improved speed range. *IEEE Transactions on Power Electronics, 19*(2), 296–302. https://doi.org/10.1109/TPEL.2003.823174
28. Zhao, S., & Fu, H. (2018). A novel vibration sensor system for frequency measurement based on Bias Flip technique. *Measurement, 124*, 56–63. https://doi.org/10.1016/j.measurement.2018.03.070
29. Hou, Y., Jiao, R., & Yu, H. (2021). MEMS based geophones and seismometers. *Sensors & Actuators Part A, 318*, 112498. https://doi.org/10.1016/j.sna.2020.112498
30. Wang, J., Hu, B., Li, W., Song, G., Jiang, L., & Liu, T. (2016). Design and application of fiber Bragg grating (FBG) geophone for higher sensitivity and wider frequency range. *Measurement, 79*, 228–235. https://doi.org/10.1016/j.measurement.2015.09.041
31. Zhang, X., Liu, X., Zhang, F., Sun, Z., Min, L., Li, S., Jiang, S., Li, M., Wang, C., & Ni, J. (2018). Reliable high sensitivity FBG geophone for low frequency seismic acquisition. *Measurement, 129*, 62–67. https://doi.org/10.1016/j.measurement.2018.07.009
32. Lee, S. H., & Lee, S. (2022). Fabrication of comb-structured acceleration sensors by roll-to-roll gravure printing. *International Journal of Precision Engineering and Manufacturing-Green Technology, 9*(2), 409–420. https://doi.org/10.1007/s40684-021-00342-7
33. So, S. Y., Park, S. H., Park, S. H., Gwak, G. M., & Lyu, S. K. (2023). Additive-manufactured flexible triboelectric sensor based on porous PDMS sponge for highly detecting joint movements. *International Journal of Precision Engineering and Manufacturing-Green Technology, 10*(1), 97–107. https://doi.org/10.1007/s40684-022-00432-0
34. Zhu, J., Sun, H., Xu, Y., Liu, T., Hou, T., Liu, L., Li, Y., Lin, T., & Xin, Y. (2019). Preparation of PVDF/TiO_2 nanofibers with enhanced piezoelectric properties for geophone applications. *Smart Materials & Structures, 28*(8), 085006. https://doi.org/10.1088/1361-665X/ab29a9
35. Ma, K., Wu, J., Ma, Y., Xu, B., Qi, S., & Jiang, X. (2023). An effective method for improving low-frequency response of geophone. *Sensors, 23*(6), 3082. https://doi.org/10.3390/s23063082
36. Kim, Y.-D., Kim, S.-Y., & Park, K.-H. (2009). Development of the six degree-of-freedom active vibration isolation system by using a phase compensated velocity sensor. *Transactions of the Korean Society of Mechanical Engineers A, 33*(11), 1347–1352. https://doi.org/10.3795/KSME-A.2009.33.11.1347
37. Aguirre, F. L., Pazos, S. M., Peretti, G., & Romero, E. A. (2016). A state-variable filter as a case study of the transient response analysis method. In *IEEE Biennial Congress of Argentina (ARGENCON), 2016*. (pp. 1–6). IEEE Publications. https://doi.org/10.1109/ARGENCON.2016.7585333
38. Kubanek, D., & Vrba, K. (2008). Second-order state-variable filter with current operational amplifiers. In *Third international conference on systems (icons 2008)* (pp. 57–61). IEEE Publications. https://doi.org/10.1109/ICONS.2008.26
39. Vural, R. A., & Yildirim, T. (2010). State variable filter design using particle swarm optimization. In *XIth international workshop on symbolic and numerical methods, modeling and applications to circuit design, 2010* (pp. 1–4). IEEE Publications. https://doi.org/10.1109/SM2ACD.2010.5672302
40. Zhang, X., Wei, X., Wang, T., Li, X., Xiao, W., & Wu, Z. (2020). A digital low-frequency geophone based on 4th-order sigma-delta modulator and single-coil velocity feedback. *Sensors & Actuators Part A, 312*, 112074. https://doi.org/10.1016/j.sna.2020.112074
41. Kim, M. H., Kim, H. Y., Kim, H. C., Ahn, D., & Gweon, D. (2016). Design and control of a 6-dof active vibration isolation system using a Halbach magnet array. *IEEE/ASME Transactions on Mechatronics, 21*(4), 2185–2196. https://doi.org/10.1109/TMECH.2016.2539349
42. Yen, J.-Y., Lan, K.-J., & Kramar, J. A. (2005). Active vibration isolation of a large stroke scanning probe microscope by using discrete sliding mode control. *Sensors & Actuators Part A, 121*(1), 243–250. https://doi.org/10.1016/j.sna.2005.02.035
43. Zhang, L.-F., Li, X., Fang, J., Lv, Y., Ma, B., Wu, J., & Li, H. (2019). Vibration isolation of extended ultra-high acceleration macro–micro motion platform considering floating stator stage. *International Journal of Precision Engineering & Manufacturing, 20*(8), 1265–1287. https://doi.org/10.1007/s12541-019-00152-7
44. Pham, M.-N., & Ahn, H.-J. (2015). Horizontal active vibration isolator (HAVI) using electromagnetic planar actuator (EPA). *International Journal of Precision Engineering & Manufacturing-Green Technology, 2*(3), 269–274. https://doi.org/10.1007/s40684-015-0032-9
45. Choi, J., Kim, K., Kim, H., & Lee, S. (2020). Effect of inertia variations for active vibration isolation systems. *Precision Engineering, 66*, 507–518. https://doi.org/10.1016/j.precisioneng.2020.07.003
46. Kumar, R., Singh, S. P., & Chandrawat, H. N. (2005). Multivariable adaptive vibration control of smart structures using iterative (LQG) control strategies. *Smart Materials & Structures, 14*(5), 953–962. https://doi.org/10.1088/0964-1726/14/5/033
47. Pota, H. R., Moheimani, S. R., & Smith, M. (2002). Resonant controllers for smart structures. *Smart Materials & Structures, 11*(1), 1.

48. Beker, M. G., Bertolini, A., van den Brand, J. F., Bulten, H. J., Hennes, E., & Rabeling, D. S. (2014). State observers and Kalman filtering for high performance vibration isolation systems. *Review of Scientific Instruments, 85*(3), 034501. https://doi.org/10.1063/1.4866659
49. Nghi, H. V., Nhien, D. P., & Ba, D. X. (2022). A lqr neural network control approach for fast stabilizing rotary inverted pendulums. *International Journal of Precision Engineering and Manufacturing, 23*, 45–56. https://doi.org/10.1007/s12541-021-00606-x

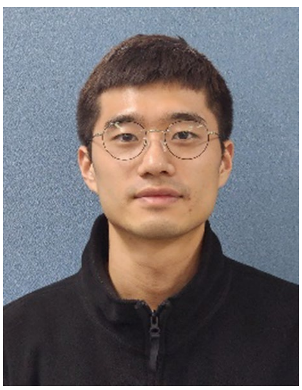

Jinsoo Choi received B.Sc. and M.Sc. in Mechatronics Engineering from Tech University of Korea, Siheung, South Korea, in 2018 and in 2020, respectively. He is on a doctoral program in the Korea Advanced Institute of Science and Technology, Daejeon, South Korea. His research has focused on design of active filter, active vibration control and dynamics of multi-body systems.

Hongki Yoo received B.S., M.S. and Ph.D. in Mechanical Engineering from Korea Advanced Institute of Science and Technology, Daejeon, South Korea in 2001, 2003 and 2007, respectively. He is associate professor of mechanical engineering in Korea Advanced Institute of Science and Technology. His research has focused on biomedical optics and optical metrology.

Eunjong Choi received B.S. in Mechatronics Engineering from Tech University of Korea, Siheung, South Korea, in 2022. He is on the master's course of mechatronics engineering in Techology University of Korea. His research has focused on active vibration control system and precision control.

Kihyun Kim received B.S., M.S. and Ph.D. degrees in mechanical engineering from the Korea Advanced Institute of Science and Technology (KAIST), Daejeon, South Korea, in 1999, 2001, and 2006, respectively. Since 2015, he has been an Associate Professor in the department of mechatronics engineering, Tech University of Korea. His current research interests include the design and control of a high-performance mechatronics system.

Dr. Hyo-Young Kim received his B.S. in mechanical engineering in 2007 from the Hanyang University, and M.S. and Ph.D. degrees in mechanical engineering from the KAIST, in 2009 and 2013. He is assistant professor of mechatronics engineering at Tech University of Korea. His research has focused on design and control of nano-precision stage.